Materials Horizons

ROYAL SOCIETY OF CHEMISTRY

COMMUNICATION

View Article Online
View Journal

Cite this: DOI: 10.1039/d6mh00067c

Received 13th January 2026,
Accepted 15th April 2026

DOI: 10.1039/d6mh00067c

rsc.li/materials-horizons

Planar rotor-enabled quenching-resistant NIR-II fluorophores for high-contrast bioimaging and efficient cancer phototheranostics

Weilong Chen,[a] Sa Wang,[b] Ganipisetti Hanumantha Rao,[c] Ka-Wai Lee,[a] Zhiqiang Guan,[a] Siyu Chen,[b] Yuqing Li,[a] Chuang Zhang,[b] Yeteng Zhong,[e] Jinfeng Zhang, *[b] Ken-Tsung Wong, *[cd] Yingpeng Wan *[a] and Chun-Sing Lee [a]

Quenching-resistant near-infrared-II (NIR-II) fluorophores with strong light harvesting capabilities and excellent photophysical properties remain a critical challenge in cancer phototheranostics. Herein, we report a novel acceptor–donor–acceptor (A–D–A) fluorophore, BTP-2TCF, constructed by introducing planar, rotatable tricyanofuran (TCF) acceptors into the core of the high-performance dye Y6. This molecular design imparts obvious anti-quenching behavior to BTP-2TCF nanoparticles (NPs), achieving an improved photoluminescence quantum yield of 1.9% and over a ten-fold enhancement in reactive oxygen species generation compared to Y6 NPs. These improvements are likely attributed to the restricted intramolecular motion of the TCF rotor, which suppresses non-radiative energy dissipation. BTP-2TCF NPs also exhibit a high molar absorption coefficient ($>82\,000$ M^{-1} cm^{-1}) and brightness (635 M^{-1} cm^{-1}), outperforming conventional anti-quenching dyes. Their bright NIR-II fluorescence enables high-contrast visualization of mouse vasculature. Guided by NIR-II fluorescence imaging, BTP-2TCF NPs demonstrate superior photodynamic and photothermal anticancer efficacy *in vivo*. This study highlights the TCF planar rotor as a powerful strategy for developing next-generation quenching-resistant fluorophores for biomedical applications.

New concepts

This work presents a novel molecular design strategy for constructing quenching-resistant near-infrared-II (NIR-II) fluorophores that simultaneously exhibit high fluorescence brightness and efficient reactive oxygen species (ROS) generation. Traditional planar fluorophores offer strong emission but suffer from severe quenching in the aggregated nanoparticle (NP) state. In contrast, aggregation-induced emission (AIE) fluorophores maintain emission in aggregates but often compromise absorption due to their twisted molecular structures. To overcome this trade-off, we introduce a planar tricyanofuran (TCF) rotor design that integrates molecular planarity with rotational flexibility. This unique structure enables a high molar absorption coefficient, excellent NIR-II quantum yield and ROS yield. Upon aggregation, the rotor's motion is restricted, suppressing nonradiative decay and enhancing both fluorescence and ROS generation. The resulting BTP-2TCF nanoparticles demonstrate outstanding photophysical properties, including a high absorption coefficient (82 000 M^{-1} cm^{-1}), and excellent fluorescence quantum yield (1.9%) and ROS production, achieving an ultrahigh NIR-II brightness (635 M^{-1} cm^{-1}) that surpasses existing fluorophores. This planar rotor concept offers a transformative approach for designing high-performance, quenching-resistant organic fluorophores, advancing the development of next-generation NIR-II imaging and therapy agents.

1. Introduction

Effective cancer treatment remains a formidable challenge due to the intrinsic limitations of conventional therapies, which are typically marked by limited specificity, systemic toxicity, and poor integration with diagnostic tools.[1–4] The emergence of second near-infrared (NIR-II, 900–1700 nm) fluorescence imaging-guided phototheranostics particularly has opened new avenues for precision oncology.[5–8] NIR-II fluorescence imaging offers deep tissue penetration, high spatial resolution, and minimal background interference, enabling accurate tumor visualization and real-time therapeutic guidance.[9–11] When combined with photodynamic therapy (PDT) and photothermal therapy (PTT), this approach facilitates synergistic tumor ablation with reduced off-target effects, thereby

[a] Center of Super-Diamond and Advanced Films (COSDAF), Department of Chemistry, City University of Hong Kong, 83 Tat Chee Avenue, Kowloon, Hong Kong SAR 999077, P. R. China. E-mail: ypwan3@cityu.edu.hk
[b] Key Laboratory of Molecular Medicine and Biotherapy, School of Life Science, Beijing Institute of Technology, Beijing 100081, P. R. China. E-mail: jfzhang@bit.edu.cn
[c] Department of Chemistry, National Taiwan University, Taipei 10617, Taiwan. E-mail: kenwong@ntu.edu.tw
[d] Institute of Atomic and Molecular Science, Academia Sinica, Taipei 10617, Taiwan
[e] CAS Key Laboratory for Biomedical Effects of Nanomaterials and Nanosafety, CAS Center for Excellence in Nanoscience, National Center for Nanoscience and Technology, Chinese Academy of Sciences, Beijing 100190, P. R. China

enhancing therapeutic precision and minimizing systemic toxicity.[12–14]

To harness the full potential of NIR-II fluorescence imaging in phototheranostics, a wide array of materials have been developed.[13,15,16] Inorganic nanomaterials–such as quantum dots, rare-earth-doped nanoparticles (NPs), and single-walled carbon nanotubes–have garnered considerable attention owing to their intense NIR-II fluorescence and high photothermal conversion efficiency (PCE). However, their clinical translation remains limited by concerns over long-term biocompatibility and inefficient body clearance.[15–19] These limitations have prompted growing interest in organic small-molecule fluorophores, which offer several intrinsic advantages, including near-infrared (NIR) absorption, bright NIR-II emission, efficient reactive oxygen species (ROS) and heat generation under NIR irradiation, as well as favorable biocompatibility and clearance profiles.[17–19]

To achieve long-wavelength absorption and emission, organic NIR-II fluorophores typically require extended π-conjugated systems and planar molecular backbones.[20–22] These structural features facilitate red-shifted optical properties by narrowing the energy gap between the highest occupied and lowest unoccupied molecular orbitals (HOMO–LUMO).[23,24] However, such molecular designs are inherently prone to strong π–π stacking in the aggregated state, often resulting in aggregation-caused quenching (ACQ).[25–27] ACQ significantly diminishes both fluorescence intensity and ROS generation efficiency, thereby undermining the dual imaging and therapeutic functionalities essential for effective phototheranostics.[28–30]

To overcome this limitation, considerable attention has been directed toward the development of quenching-resistant NIR-II fluorophores that retain or even enhance their photophysical properties upon aggregation.[31,32] In this regard, aggregation-induced emission (AIE) fluorophores have emerged as a transformative class of materials.[33–36] Unlike conventional fluorophores, AIE-active molecules exhibit minimal emission in the molecularly dispersed state but become highly emissive upon aggregation. This unique behavior is attributed to the restriction of intramolecular motions of rotors in the aggregated state, which suppresses nonradiative decay pathways and promotes radiative transitions.[37,38] AIE fluorophores often incorporate twisted molecular architectures with rotatable donor units such as triphenylamine (TPA) or tetraphenylethylene (TPE), which effectively inhibit π–π stacking and facilitate strong NIR-II emission and enhanced ROS generation in the aggregated NP form, making them promising candidates for phototheranostic applications.[39,40] At present, the available rotor systems are restricted to TPA and TPE, highlighting the need for broader exploration of alternative rotor candidates. To address this limitation, we propose a novel molecular design strategy based on the planar tricyanofuran (TCF) rotor. While the planar TCF rotor offers the potential for high absorption coefficients and quenching resistance, their applications in NIR-II phototheranostics remain largely unexplored.

As shown in Fig. 1, we selected the planar small molecule Y6 (BTP-4F)–previously reported for its excellent light-harvesting ability and promising phototheranostic properties–as a model system.[41–46] To enhance molecular flexibility and photophysical performance, we explored several potential electron acceptors commonly used in fused-ring conjugated small molecules as potential rotor units to replace the 2FIC acceptor in Y6 (Fig. S1, SI). Although the malononitrile acceptor offers planarity, its double bond cannot rotate and its weak electron-accepting capability limits NIR absorption. In contrast, IC-based units exhibit stronger electron-withdrawing characteristics but suffer from restricted rotation due to S–O electrostatic locking and steric hindrance from side chains.

To overcome these limitations, we introduced the TCF unit, which features an extended single bond that facilitates rotational motion while retaining strong electron-accepting properties. By substituting the electron-withdrawing 2-(5,6-difluoro-3-oxo-2,3-dihydro-1*H*-inden-1-ylidene)malononitrile (2FIC) unit in Y6 with a rotatable and planar TCF moiety, we successfully synthesized a new molecule, BTP-2TCF. In contrast to rigid acceptors such as 2FIC, the TCF unit enables free rotation in the molecular state, thereby enhancing molecular flexibility.[47] The resulting BTP-2TCF NPs exhibit a high molar absorption coefficient (82 000 M^{-1} cm^{-1} at 628 nm in water) and quenching-resistant properties, both advantageous for biomedical applications. Compared to Y6 NPs, BTP-2TCF NPs demonstrate a significantly enhanced NIR-II photoluminescence quantum yield (1.9% *vs.* 1.2% of Y6 NPs) and over a tenfold increase in ROS generation (10-fold *vs.* 1-fold of Y6 NPs), confirming its superior anti-quenching performance. Furthermore, BTP-2TCF NPs exhibit a high NIR-II brightness of 635 M^{-1} cm^{-1}, defined as the product of the molar absorption coefficient at the excitation wavelength and the fluorescence quantum yield, which markedly surpasses those of previously reported quenching-resistant NIR-II fluorophores (Table S1). This enhancement is attributed to the TCF unit, which may function as a planar rotor that rotates freely in the monomeric state but becomes inhibited upon aggregation,[48] thereby suppressing nonradiative decay while preserving both NIR-II fluorescence and ROS generation. Compared to conventional AIE-based NIR-II phototheranostic agents with twisted donor structures, our BTP-2TCF NPs combine a high absorption coefficient, bright NIR-II emission, and efficient ROS generation, offering enhanced imaging brightness and therapeutic efficacy (Fig. S2 and Table S1). Thus, this planar TCF rotor design represents an effective strategy for the development of high-performance, quenching-resistant NIR-II fluorophores for cancer phototheranostics.

2. Results

2.1. Design, synthesis, and characterization of the molecule

Stemmed from the Y6 core, a novel NIR fluorescent dye, BTP-2TCF, is synthesized and characterized. BTP-2TCF is prepared in a high yield of 62% *via* Knoevenagel condensation (Scheme S1).[49–51]

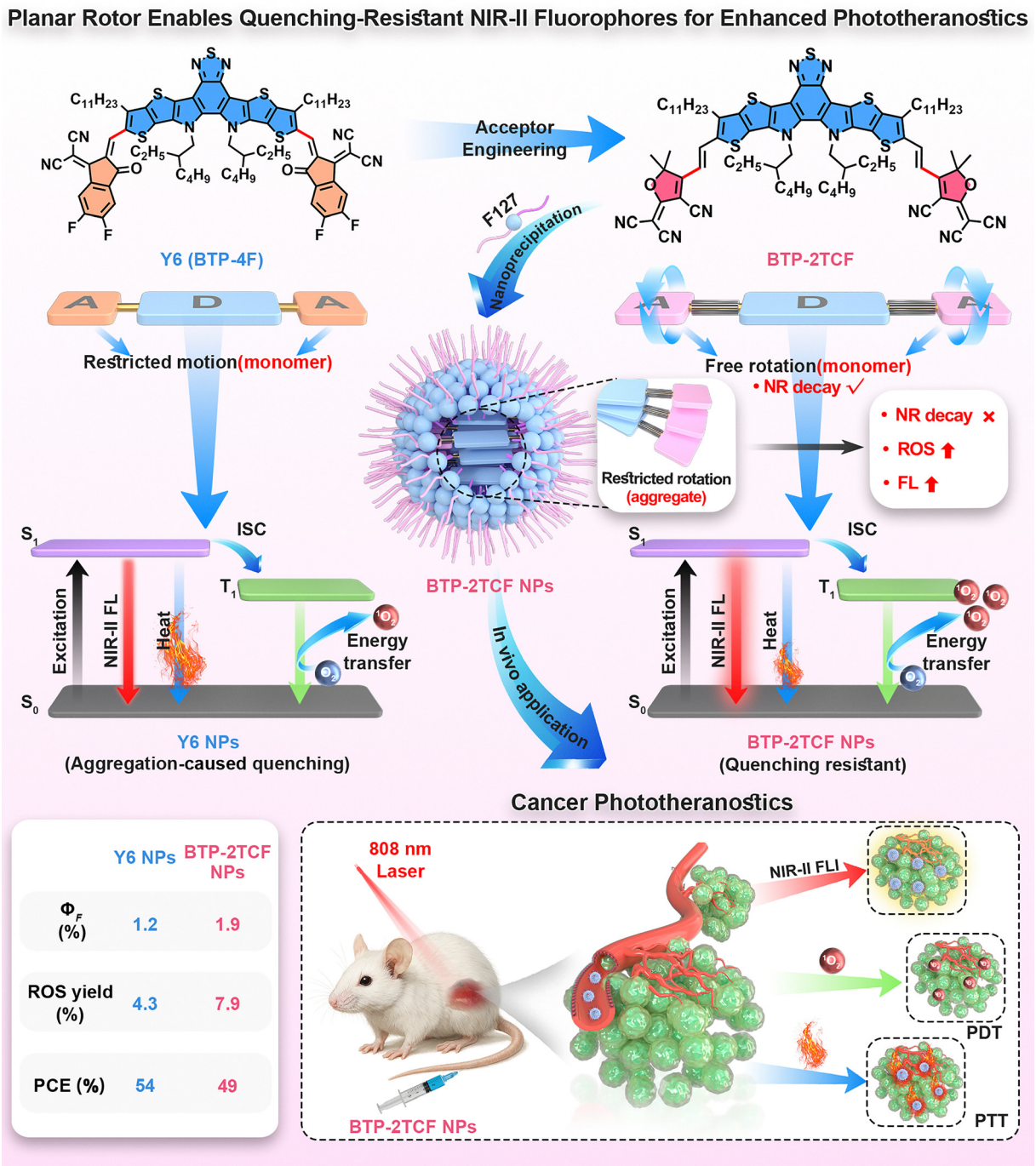

Fig. 1 Schematic illustration of the planar and rotatable tricyanofuran acceptor, enabling the development of quenching-resistant NIR-II fluorophores for cancer phototheranostics.

Its molecular structure is confirmed using nuclear magnetic resonance (NMR) spectroscopy and high-resolution mass spectrometry (HRMS) (Fig. S3–S5). To elucidate the electronic and structural properties of Y6 and BTP-2TCF, density functional theory (DFT) calculations are employed. As shown in Fig. 2A, the incorporation of the planar TCF structure lowers the energy level of the HOMO, thereby increasing the energy gap between the HOMO and the LUMO. This effect is due to the slightly twisted dihedral angle of 0.37° for BTP-2TCF (Fig. 2A and Fig. S6) compared to 0.04° for Y6, which reduces effective electron delocalization across the conjugated system.[52] Consequently, compared with Y6, BTP-2TCF exhibits a blue-shifted absorption profile along with a decreased molar extinction coefficient (99 800 M^{-1} cm^{-1} in THF) (Fig. 2B and Fig. S7). Although the molar extinction coefficient of BTP-2TCF is reduced, it remains significantly higher than that of

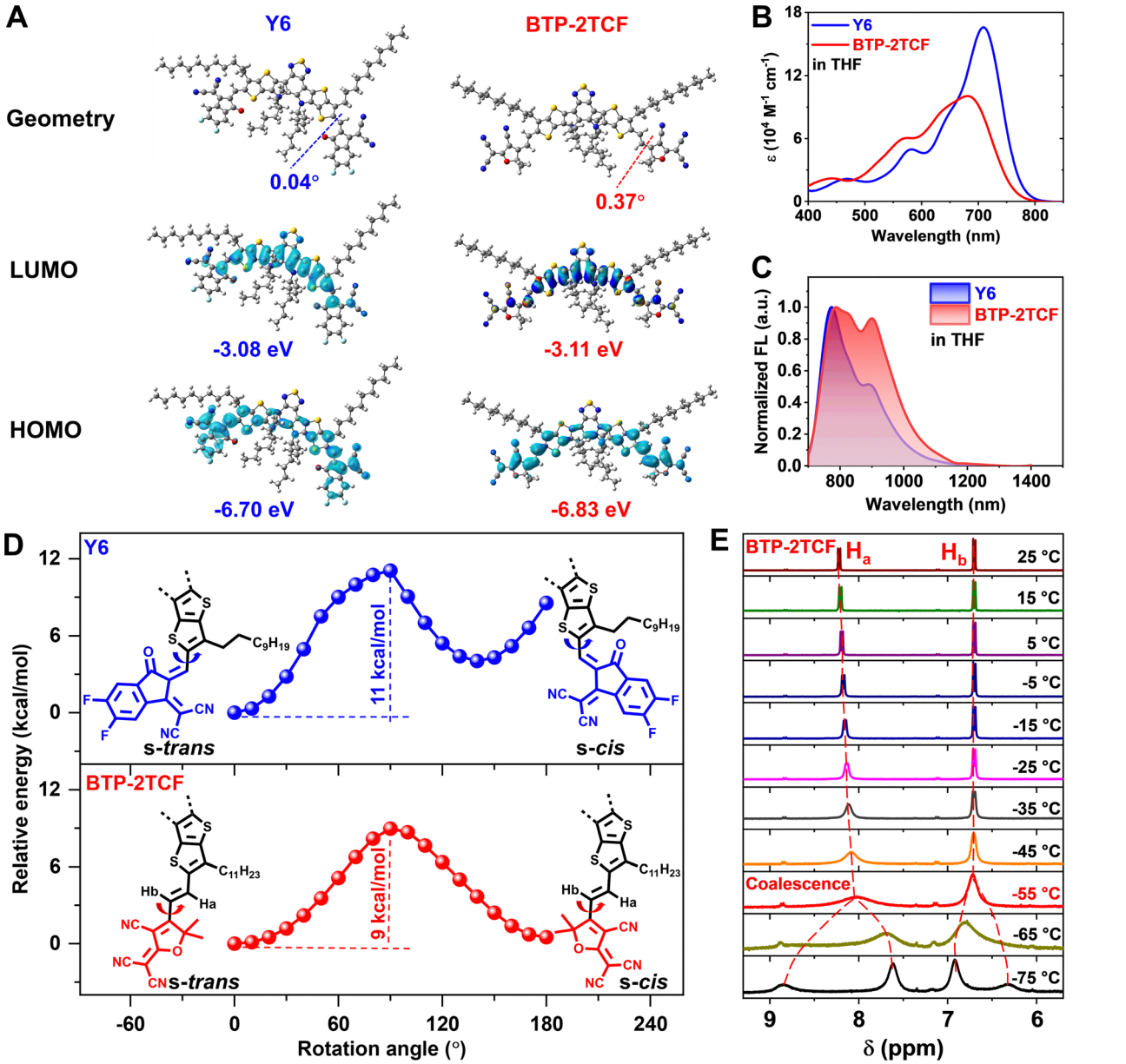

Fig. 2 Structural characterization, theoretical calculations, and optical properties of Y6 and BTP-2TCF. (A) Optimized molecular geometries and HOMO and LUMO distributions of Y6 and BTP-2TCF at the M06-2X/6-311G(d) level of theory. (B) UV-vis-NIR absorption spectra of Y6 and BTP-2TCF in THF. (C) Normalized fluorescence spectra of Y6 and BTP-2TCF in THF. (D) Dihedral angle energy scans of Y6 and BTP-2TCF using the basic set of M06-2X/6-311G (d). (E) Temperature-dependent ^{1}H NMR spectrum of the aromatic region of BTP-2TCF (600 MHz, CD_2Cl_2).

conventional quenching-resistant dyes ($<30\,000\ M^{-1}\ cm^{-1}$).[53–55] Moreover, the normalized emission spectra in tetrahydrofuran (THF) (Fig. 2C) demonstrate that both compounds display obvious emission in the NIR-II region. To investigate the rotational freedom of the single bonds in both Y6 and BTP-2TCF, we perform dihedral energy scans from the s-*cis* conformation (where the two double bonds are *cis* relative to the intervening single bond) to the s-*trans* conformation (where the double bonds adopt a *trans* arrangement).[56] It should be emphasized that these conformational isomers are not fixed geometries but exist in dynamic equilibrium due to the rotational flexibility of the single bond. As illustrated in Fig. 2D, Y6 exhibits two energy minima at 0° and 140°, with an associated energy barrier of approximately 11 kcal mol^{-1}. In contrast, BTP-2TCF maintains its lowest energy at 0° and 180°, respectively, with energy barriers of only about 9 kcal mol^{-1}. These results suggest that the incorporation of the TCF moiety increases the backbone's susceptibility to thermal perturbations, thereby enhancing its tendency for torsional twisting. Moreover, the significant energy difference observed between the s-*trans* and s-*cis* conformations highlights the relatively rigid and planar nature of the Y6 backbone. The dynamic behaviors of acceptor units for Y6 and BTP-2TCF are further investigated using temperature-dependent ^{1}H NMR spectroscopy in deuterated

dichloromethane.[47,57,58] For BTP-2TCF (Fig. 2E), the sharp doublets corresponding to the vinylic protons (Fig. S8) gradually broaden as the temperature decreases. A coalescence phenomenon is observed at around −55 °C, indicating that the rotational frequency of the TCF units approaches the NMR timescale. Upon further cooling, distinct sets of signals emerge, confirming the presence of a rapid equilibrium between different conformers enabled by the rotational freedom of the TCF moieties. Conversely, Y6 shows no significant changes in its characteristic signals upon cooling, suggesting a more rigid structure (Fig. S9). These observations are consistent with the DFT calculations and support the rotatable nature of the TCF moieties in BTP-2TCF.

2.2. Preparation and characterization of NPs

Y6 and BTP-2TCF were utilized to fabricate water-dispersible NPs *via* the nanoprecipitation method for further biomedical application. NPs were prepared by self-assembling Y6/BTP-2TCF molecules with the amphiphilic Pluronic F127 polymer. Due to the amphiphilic nature of Pluronic F127 and the hydrophobic character of BTP-2TCF, the hydrophobic small molecules preferentially localize within the inner core, while the amphiphilic F127 arranges at the periphery, thereby giving rise to micelle-like aggregates. The stability of these nanoparticles is governed by a combination of noncovalent interactions, including hydrophobic effects, van der Waals forces, and π–π stacking. The drug-loading capacity of BTP-2TCF NPs was measured as 27% *via* the lyophilization method (Fig. S11). Dynamic light scattering (DLS) measurement reveals hydrodynamic diameters of approximately 70 nm (Fig. 3A), while transmission electron microscopy (TEM) images confirm the spherical morphology (Fig. S10A and D). The insets of Fig. 3A show that the NP dispersions are transparent and clear, indicating good colloidal stability. Both types of NPs maintain

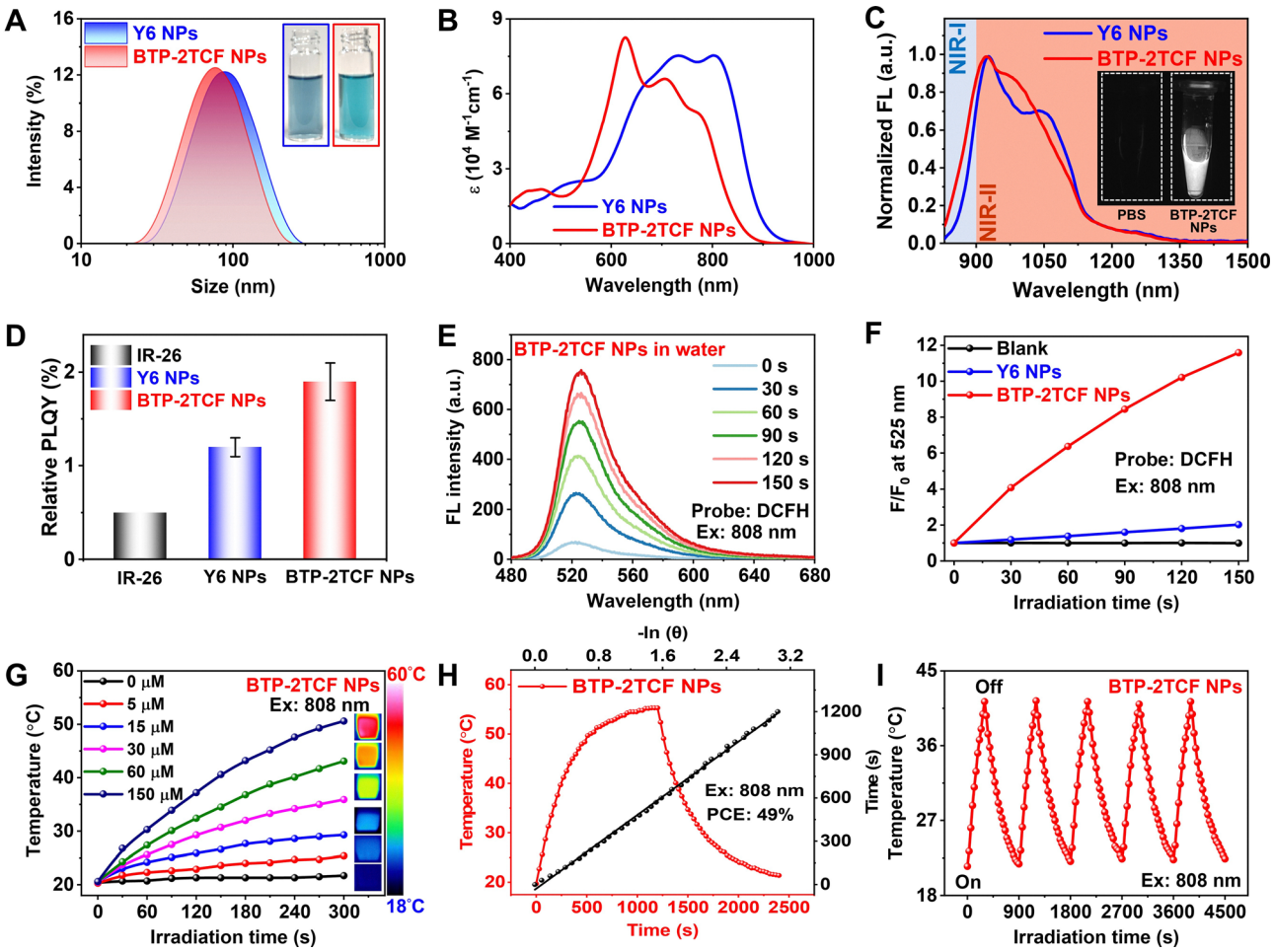

Fig. 3 Colloidal and photophysical properties of aqueous NP dispersions of Y6 and BTP-2TCF. (A) Size distribution of Y6 NPs and BTP-2TCF NPs. Insets: Photographs of the aqueous dispersions. (B) Normalized UV-vis-NIR absorption spectra of Y6 NPs and BTP-2TCF NPs. (C) Normalized fluorescence spectra of Y6 NPs and BTP-2TCF NPs. Insets: NIR-II fluorescence images of PBS and aqueous BTP-2TCF NP dispersion. (D) Relative NIR-II PLQY of Y6 NPs and BTP-2TCF NPs (reference: IR-26 in DCE with a PLQY of 0.5%). Error bars represent the standard deviation from three independent measurements. (E) Time-dependent fluorescence intensity of DCFH-DA with BTP-2TCF NPs upon 808 nm laser irradiation (500 mW cm^{-2}). (F) Comparison of fluorescence increase of DCFH alone (blank), DCFH with Y6 NPs and DCFH with BTP-2TCF NPs under 808 nm laser irradiation. (G) Temperature rise of BTP-2TCF NPs at varying concentrations after 5 minutes of laser irradiation, with corresponding infrared thermal images. (H) Heating/cooling curves and cooling time *vs.* −ln(*θ*) plot of BTP-2TCF NPs. (I) Photostability of BTP-2TCF NPs over five irradiation cycles.

stable size distributions over a period of 14 days in aqueous dispersion, further confirming their excellent colloidal stabilities (Fig. S10). The zeta potentials of BTP-2TCF NPs are measured to be −26.6 mV, which is attributed to the negatively charged F127 polymer.[59] The hydrodynamic diameters of Y6 and BTP-2TCF nanoparticles remained relatively stable over a seven day monitoring period under varying pH conditions and in phosphate-buffered saline (PBS), suggesting good colloidal stability under physiologically relevant environments (Fig. S12A–C). BTP-2TCF NPs exhibit stability in 10% fetal bovine serum (FBS) solution and efficient oxidative degradation induced by ClO^-, collectively demonstrating their favorable biodegradation potential under oxidative conditions (Fig. S12D–F). As shown in Fig. 3B, BTP-2TCF NPs exhibit strong absorption in the NIR region with high molar extinction coefficients at 808 nm of 33 400 M^{-1} cm^{-1}, suggesting their suitability for phototheranostic applications under 808 nm irradiation. Concurrently, the fluorescence spectra of NPs display prominent emission beyond 900 nm (Fig. 3C). The inset of Fig. 3C presents the NIR-II fluorescence image of BTP-2TCF NPs obtained using an InGaAs camera, highlighting their potential for NIR-II bioimaging. The photophysical parameters of Y6 NPs and BTP-2TCF NPs in water are summarized in Table S2.

The relative PLQYs of Y6 NPs and BTP-2TCF NPs were measured using IR-26 (PLQY = 0.5% in 1,2-dichloroethane (DCE)) as a reference (Fig. S13–S15).[60] Each experiment was repeated three times independently to obtain an averaged result. As illustrated in Fig. 3D, Y6 NPs show a PLQY of 1.2 ± 0.1%, while BTP-2TCF NPs display an improved value of 1.9 ± 0.2%. The generation of ROS, including singlet oxygen ($^1O_2$) superoxide radicals ($O_2^{-\bullet}$) and hydroxyl radicals ($^\bullet OH$), is further investigated for Y6 and BTP-2TCF molecules.[61] As shown in Fig. S16, the absorption of the 1,3-diphenylisobenzofuran (DPBF) probe at 415 nm significantly decreased for both Y6 and BTP-2TCF molecules compared with the blank group, indicating substantial $^1O_2$ generation. Subsequently, dihydrorhodamine 123 (DHR123) and hydroxyphenyl fluorescein (HPF) are employed to evaluate the generation of superoxide radicals and hydroxyl radicals, respectively.[62] As depicted in Fig. S17, neither the DHR123 group nor HPF group exhibited any observable fluorescence enhancement under 750 nm laser irradiation, suggesting negligible superoxide and hydroxyl radicals generation by Y6 and BTP-2TCF molecules. Furthermore, the overall ROS-generation capacity of Y6 and BTP-2TCF NPs is assessed using the ROS fluorescent probe of 2′,7′-dichlorodihydrofluorescin (DCFH). As depicted in Fig. 3E and Fig. S18, BTP-2TCF NPs demonstrate a pronounced fluorescence rise in the presence of DCFH, whereas Y6 NPs exhibit only a modest increase under identical conditions (Fig. S18B). As summarized in Fig. 3F, the NIR-triggered ROS generation of BTP-2TCF NPs is approximately 10.2 times greater than that of Y6 NPs, emphasizing the superior PDT efficacy of BTP-2TCF NPs.

The photothermal properties of Y6 and BTP-2TCF NPs are systematically evaluated using an 808 nm laser with a power density of 1 W cm^{-2}. As illustrated in Fig. 3G, temperature increments in BTP-2TCF NP dispersions at various concentrations are recorded under 300 s of laser irradiation. Notably, exposure to laser irradiation for 5 minutes results in a temperature increase to approximately 50 °C in a dispersion containing 150 μmol L^{-1} NPs, highlighting the potential of BTP-2TCF NPs for PTT applications. Based on previous reported methods,[63,64] the photothermal conversion efficiency (η, PCE) of BTP-2TCF NPs is determined to be 49% (Fig. 3H and Table S2). Additionally, the photothermal stability of BTP-2TCF NPs is investigated through five consecutive heating and cooling cycles. As depicted in Fig. 3I, the temperature profile of BTP-2TCF NPs remains consistent across all five excitation cycles under 808 nm laser irradiation, demonstrating their remarkable stability and suitability for biomedical applications. For comparative analysis, the photothermal properties of Y6 NPs are also examined (Fig. S19). Y6 NPs exhibit similar temperature increases at different concentrations under 808 nm laser irradiation and display comparable thermal stability over five repeated heating and cooling cycles. The PCE of Y6 NPs is measured to be 54%, slightly higher than 49% observed for BTP-2TCF NPs. This difference may be attributed to the less efficient energy transfer pathways in BTP-2TCF NPs, where a greater proportion of absorbed energy is funneled into ROS generation and fluorescence rather than heat production.

2.3. Quenching-resistant analysis

When NIR-II fluorophores aggregate into NPs, strong π–π stacking interactions often lead to significant quenching of both fluorescence and ROS generation.[65,66] In this study, the quenching-resistant properties of the developed NPs are investigated. In this study, the quenching-resistant properties of the developed molecules are investigated. To elucidate their aggregation behavior, powder X-ray diffraction (XRD) measurements were conducted on the corresponding solids.[67–70] As illustrated in Fig. S20, the diffraction peak of BTP-2TCF at 22.9° corresponds to a *d*-spacing of 0.387 nm, as calculated using Bragg's law. In comparison, Y6 exhibits a smaller *d*-spacing of 0.346 nm, indicating its more compact molecular packing in the solid state. Although BTP-2TCF exhibits relatively looser packing, the intermolecular distances remain sufficiently short to suggest that the rotational motion of the TCF units may be restricted upon aggregation. Attempts to grow single crystals of BTP-2TCF were unsuccessful, likely due to the high conformational flexibility of the acceptor in solution. Complementary molecular dynamics simulations were also performed; however, the results proved inconclusive and did not fully align with the experimental observations.

The Method of Moments is used to calculate the oscillator strengths (f) from the absorption spectra of both the molecular state and NPs' dispersions (Fig. 4A).[71] Upon transitioning from THF solution to NPs' dispersion, the f of Y6 decreases from 2.33 to 1.65, while that of BTP-2TCF decreases only slightly from 1.97 to 1.69. Since strong π–π stacking typically leads to a substantial reduction in absorption intensity, the smaller decrease observed for BTP-2TCF implies weaker intermolecular interactions and enhanced resistance to ACQ.[72] The differences

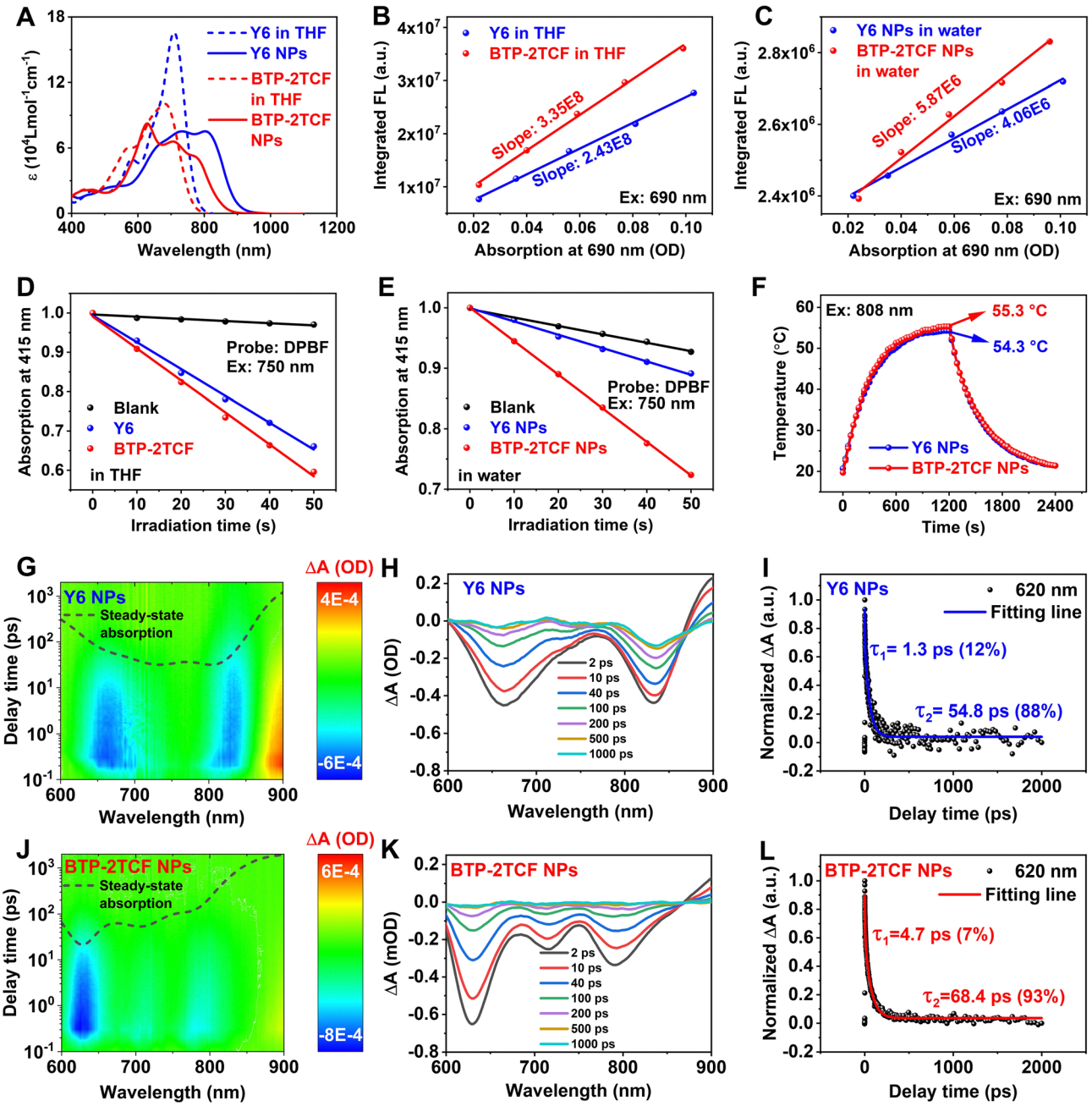

Fig. 4 Quenching-resistant properties of fluorescence and singlet oxygen generation and excited-state dynamics of Y6 and BTP-2TCF NPs. (A) UV-vis-NIR absorption spectra of Y6 and BTP-2TCF in THF, and their corresponding NPs in water. (B) Plots of integrated fluorescence intensities (700–1300 nm) of Y6 and BTP-2TCF in THF at five concentrations. (Based on the Least Squares Method; R^2: 0.997 for Y6 and 0.997 for BTP-2TCF.) (C) Plots of integrated fluorescence intensities (700–1300 nm) of Y6 NPs and BTP-2TCF NPs in water at five concentrations. (Based on the Least Squares Method; R^2: 0.995 for Y6 NPs and 0.990 for BTP-2TCF NPs.) (D) Singlet oxygen generation detected by time-dependent absorption changes of the DPBF probe with/without Y6 and BTP-2TCF in THF under 750 nm laser excitation (160 mW cm^{-2}). (Based on the Least Squares Method; R^2: 0.944 for blank, 0.996 for Y6, and 0.997 for BTP-2TCF.) (E) Singlet oxygen generation detected by time-dependent absorption changes of the DPBF probe with/without Y6 and BTP-2TCF NPs in water under 750 nm laser excitation (160 mW cm^{-2}). (Based on the Least Squares Method; R^2: 0.994 for blank, 0.997 for Y6 NPs, and 1.000 for BTP-2TCF NPs.) (F) Heating and cooling curves of Y6 and BTP-2TCF NPs with the same absorption intensities at 808 nm under 808 nm laser irradiation. (G) 2D pseudo-color fs-TA spectra of Y6 NPs excited by a 700 nm pump pulse. (H) fs-TA plots of Y6 NPs at different delay times. (I) Normalized kinetic decay curve and fitted line of the transient absorption signal at 620 nm for Y6 NPs. (J) 2D pseudo-color fs-TA spectra of BTP-2TCF NPs excited by a 700 nm pump pulse. (K) fs-TA plots of BTP-2TCF NPs at different delay times. (L) Normalized kinetic decay curve and fitted line of the transient absorption signal at 620 nm for BTP-2TCF NPs.

in PLQY between the molecular state and the nanoparticle state were further investigated under 690 nm xenon light excitation, a wavelength specifically chosen in view of the negligible absorption of the molecules in THF at 808 nm (see Fig. 4A).

As shown in Fig. 4B and Fig. S21, the PLQY of BTP-2TCF in THF is approximately 1.38 times higher than that of Y6. Upon NPs' formation, both Y6 and BTP-2TCF exhibit PLQY reductions exceeding 95% (Fig. 4C and Fig. S22). Notably, BTP-2TCF NPs retain a PLQY that is 1.45 times higher than that of Y6 NPs in aqueous media. As shown in Fig. S23, the absolute PLQY of Y6 decreases by 93% upon nanoparticle formation (from 2.67% for molecules to 0.2% for NPs). In contrast, BTP-2TCF exhibits a smaller decline of only 80% (from 3.51% to 0.7%). This notably higher retention of emission efficiency directly demonstrates the superior anti-quenching ability of BTP-2TCF. Although direct experimental evidence for restriction of the rotatable TCF moiety in aggregates remains challenging, we measured emission spectra of Y6 and BTP-2TCF in THF/DMSO mixtures with varying DMSO fractions (f_{DMSO}). As shown in Fig. S24 and S25, increasing f_{DMSO} leads to progressive fluorescence weakening and enhanced hydrodynamic size, consistent with QY measurements. Notably, the fluorescence change of BTP-2TCF upon aggregation was smaller than that of Y6, especially when f_{DMSO} is over 70%, suggesting that BTP-2TCF exhibits resistance to aggregation-induced quenching. As shown in Fig. S26, the temperature-dependent PL lifetimes of BTP-2TCF reveal a significant increase from 0.954 ns at room temperature to 2.580 ns at low temperature. This prolonged lifetime indicates the suppression of molecular motions, including rotation, which consequently favors radiative decay pathways. These findings collectively suggest that the observed anti-quenching behavior is most likely attributable to the restricted intramolecular motion of the TCF rotor in the aggregated state at low temperatures.

The ROS generation capacities of monomers in THF and NPs in water are compared using the DPBF probe under identical conditions. Samples are irradiated at 750 nm, as Y6 and BTP-2TCF molecules show negligible absorption at 808 nm. As illustrated in Fig. 4D and Fig. S14, the absorbance of the DPBF probe decreases similarly in the presence of Y6 and BTP-2TCF monomers, indicating comparable singlet oxygen generation efficiencies. Under the same conditions, the DPBF absorbance in the presence of BTP-2TCF NPs shows a clear decrease, with only a 20% reduction rate compared to the monomeric form (Fig. 4E and Fig. S27). In contrast, Y6 NPs exhibit a much smaller decrease in DPBF absorbance, corresponding to a $\sim$51% reduction in singlet oxygen generation efficiency relative to the Y6 monomer. These results indicate that while Y6 suffers from severe ACQ of ROS generation, BTP-2TCF maintains high ROS output in the aggregated state. This quenching-resistant behavior endows BTP-2TCF NPs with excellent ROS generation capabilities, making them promising candidates for PDT applications.

Similarly to their NIR-II fluorescence, the quenching-resistant ROS generation of BTP-2TCF NPs is likely attributed to the restricted intramolecular motion of the planar TCF rotor in the aggregated state. Such restriction facilitates excited-state energy dissipation through both fluorescence emission and ROS generation.[73] This mechanism resembles the well-known AIE phenomenon. However, the TCF rotor introduced here offers improved planarity compared to conventional TPA and TPE rotors. This novel design not only addresses the low absorption coefficient issue of traditional AIE fluorophores but also retains their quenching-resistant properties. The TCF-rotor strategy thus presents a promising avenue for developing next-generation quenching-resistant fluorophores.[74]

The singlet oxygen quantum yields (Φ_Δ) of the developed NPs were evaluated using DPBF as a trapping probe and ICG as a reference (Φ_Δ = 0.2%).[75–77] As shown in Fig. S28, both Y6 NPs and BTP-2TCF NPs exhibit markedly higher singlet-oxygen generation efficiencies than ICG. Notably, the Φ_Δ of BTP-2TCF NPs (7.9%) is approximately 1.8-fold higher than that of Y6 NPs (4.3%). The Φ_Δ values, together with the NIR-II PLQYs and PCEs of NPs, are summarized in Table S2. Overall, Y6 NPs display a higher PCE, whereas BTP-2TCF NPs demonstrate superior ROS production and PLQY. This contrasting behavior is consistent with the proposed excitation-energy redistribution pathway, in which absorbed energy is partitioned into distinct relaxation channels. Importantly, these efficiencies should not be directly summed, as excited-state relaxation comprises multiple parallel and competing processes, with additional dissipation through quantified pathways. Each reported efficiency thus represents a specific relaxation route rather than a fractional contribution to a closed energy budget.

Following assessment of the fluorescence emission and ROS generation pathways, the photothermal-induced heat generation of Y6 and BTP-2TCF NPs is further compared. As shown in Fig. 4F, the PCE of Y6 NPs is approximately 1.1 times higher than that of BTP-2TCF NPs. To elucidate the excited-state dynamics underlying this behavior, femtosecond transient absorption (fs-TA) spectroscopy is employed. The pseudo-color fs-TA spectra (Fig. 4G and J) display distinct positive and negative signal bands. The positive bands correspond to excited-state absorption (ESA), while the negative bands arise from a combination of ground-state bleaching (GSB) and stimulated emission (SE), as evidenced by their spectral alignment with the steady-state absorption and fluorescence spectra.[78–82]

All recorded signals demonstrate a gradual decay with increasing delay time (Fig. 4H and K). Among these, the GSB signal reflects the repopulation of the ground state (S_0) *via* nonradiative decay, thereby directly indicating photothermal effects. Due to the typically small Stokes shifts in organic materials, spectral overlap between SE and GSB is common. To minimize SE interference, a shorter probe wavelength of 620 nm is selected. As shown in Fig. 4I, the decay kinetics of excited Y6 NPs at 620 nm can be deconvoluted into two components: 12% of the signal decays with a lifetime (τ_1) of 1.3 ps, and 88% decays with a lifetime (τ_2) of 54.8 ps, both shorter than those observed for BTP-2TCF NPs (Fig. 4L). These shorter lifetimes are attributed to the rapid nonradiative decay process, which may contribute to the enhanced PCE of Y6 NPs.

2.4. *In vitro* phototherapeutic performance

Given their superior ROS generation capability, BTP-2TCF NPs are selected for further *in vitro* photodynamic and

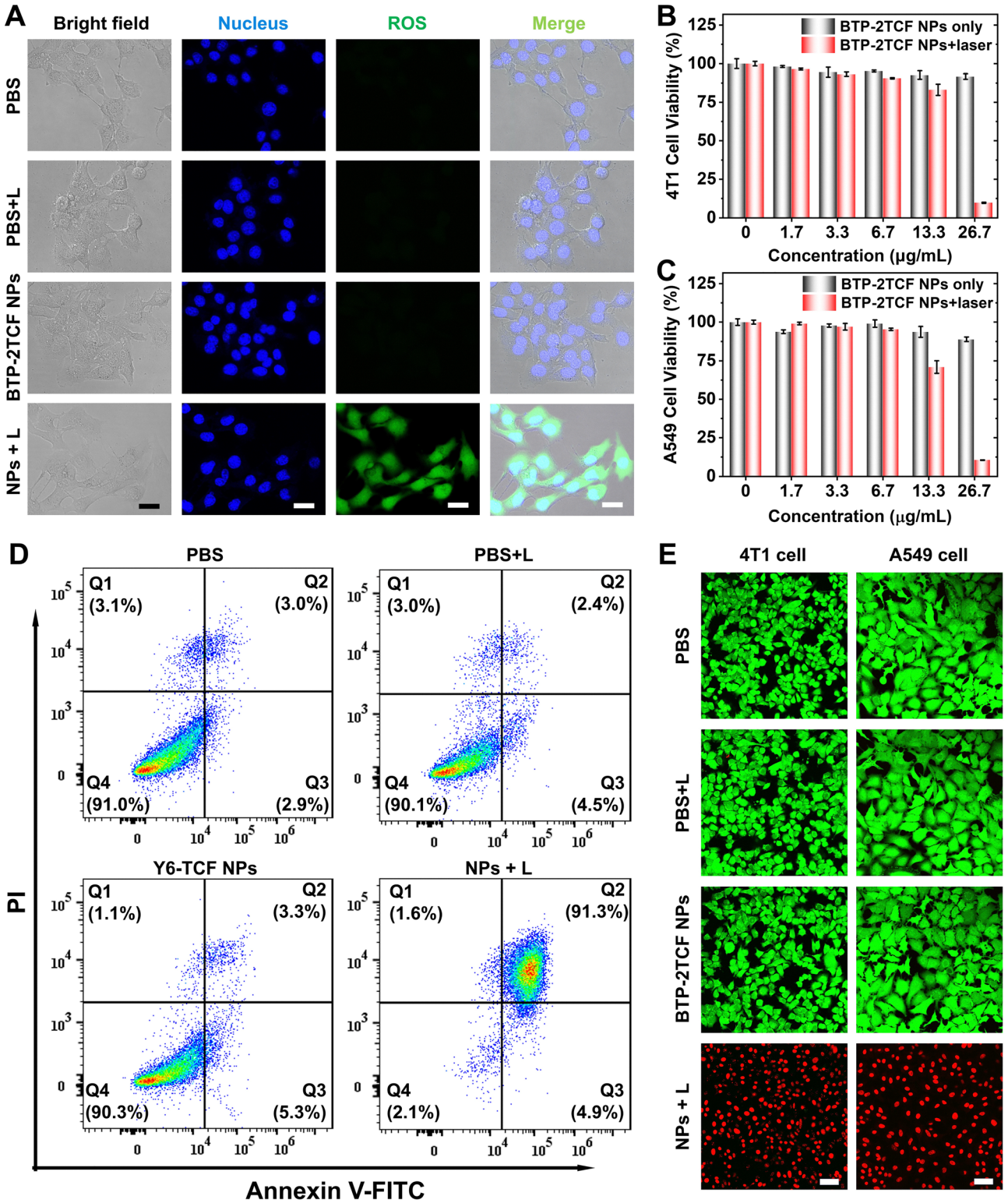

Fig. 5 *In vitro* phototherapeutic performance of BTP-2TCF NPs. (A) Confocal fluorescence images of ROS generation in 4T1 cells under various treatment conditions. Probes: DCFH-DA for ROS detection and Hoechst 33342 for nuclear staining. Scale bar: 25 μm. (B) Cell viability of 4T1 cells treated with varying concentrations of BTP-2TCF NPs with or without 808 nm laser irradiation (1 W cm^{-2}, 5 min). Data are presented as mean ± standard deviation (n = 4). (C) Cell viability of A549 cells treated with varying concentrations of BTP-2TCF NPs with or without 808 nm laser irradiation (1 W cm^{-2}, 5 min). Data are presented as mean ± standard deviation (n = 4). Data are presented as mean ± standard deviation. (D) Flow cytometry analysis of apoptosis and necrosis in 4T1 cells following different treatments. (E) Live-dead cell imaging of A549 cells stained with calcein-AM and ethidium homodimer-1 under various treatment conditions. Scale bar: 50 μm.

photothermal therapy studies in cancer cells. Intracellular ROS generation is first assessed using DCFH-DA as a fluorescent probe, alongside Hoechst 33342 staining for nuclear visualization. As shown in Fig. 5A, no green fluorescence indicative of oxidized DCF is observed in 4T1 cancer cells treated with PBS alone, PBS with laser irradiation (PBS + L) or BTP-2TCF NPs without irradiation. In contrast, cells incubated with BTP-2TCF NPs and subjected to laser irradiation (NPs + L) exhibit strong green fluorescence, confirming efficient intracellular ROS production. A comparative *in vitro* study of Y6 NPs and BTP-2TCF NPs (Fig. S29 and S30) shows that BTP-2TCF NPs possess markedly enhanced ROS-generating capability and superior PDT efficacy. Specifically, intracellular ROS imaging using DCFH-DA in 4T1 cells under 808 nm irradiation revealed significantly stronger green fluorescence in the BTP-2TCF NP group, indicating more efficient ROS production. Furthermore, CCK-8 assays confirmed that under identical treatment conditions, BTP-2TCF NPs induced more pronounced cytotoxicity than Y6 NPs. Collectively, these results demonstrate that our newly developed BTP-2TCF NPs exhibit substantially improved PDT performance. Furthermore, cytotoxicity assays in 3T3 normal cells under dark conditions at various NP concentrations reveal no observable toxicity, even at concentrations as high as 100 μg mL^{-1}, highlighting the excellent biocompatibility of BTP-2TCF NPs (Fig. S31). The anti-cancer efficacy of BTP-2TCF NPs is further evaluated using a CCK8 assay in 4T1 and A549 cancer cell lines.

As shown in Fig. 5B, the viability of 4T1 cells decreased significantly to approximately 10% following treatment with 26.7 μg mL^{-1} BTP-2TCF NPs under 808 nm laser irradiation, whereas cells treated with NPs alone exhibit only a slight decrease in viability. A similar trend is observed in A549 cells (Fig. 5C). These results demonstrate that BTP-2TCF NPs are highly effective for NIR light-activated phototherapy across different cancer cells types with minimal dark toxicity. In the dark-toxicity assays, 3T3 cells showed negligible toxicity, whereas 4T1 cells exhibited obviously higher sensitivity. This difference may be attributed to inherent biological distinctions between normal and cancer cells, including greater membrane permeability, elevated metabolic activity, and enhanced endocytic capacity in cancer cells, which collectively promote higher intracellular uptake of the nanoparticles and thus greater susceptibility.

To further evaluate cell apoptosis during phototherapy, flow cytometry analysis is performed using an Annexin V-FITC/PI apoptosis detection kit (Fig. 5D). In line with the CCK8 results, both the control and NPs-only groups maintain high 4T1 cell viability, exceeding 90%. In contrast, the BTP-2TCF NPs + L group exhibits significant cellular apoptosis, with an apoptotic rate of 96.2%, indicating highly effective phototherapeutic activity. Additionally, the anticancer efficacy of BTP-2TCF NPs is assessed *via* live/dead cell staining. Calcein-AM is used to stain the cytoplasm of viable cells (green), while ethidium homodimer-1 stains the nuclei of dead cells (red). As depicted in Fig. 5E, both 4T1 and A549 cells exhibit bright green fluorescence in the PBS-only, PBS + L, and BTP-2TCF NPs only-groups, indicating minimal cytotoxicity under these conditions. In contrast, cells in the BTP-2TCF NPs + L group show strong red nuclear fluorescence, highlighting the exceptional photodynamic and photothermal anticancer effects on the NPs.

2.5. *In vivo* NIR-II fluorescence imaging and phototherapeutic efficacy

Y6 NPs were not included for *in vivo* comparison because their distinct molecular structure would lead to different pharmacokinetics and tumor-accumulation behavior,[12,83] introducing confounding factors unrelated to their photophysical properties; therefore, *in vivo* evaluation was focused solely on BTP-2TCF NPs. Fig. 6 demonstrates the clear visualization of mouse vasculature following intravenous tail injection of BTP-2TCF nanoparticles, captured using various long-pass (LP) filters. As the LP filter wavelength increases from 900 nm to 1100 nm, image contrast obviously enhances while background noise is diminished. Furthermore, cross-sectional intensity profiles of

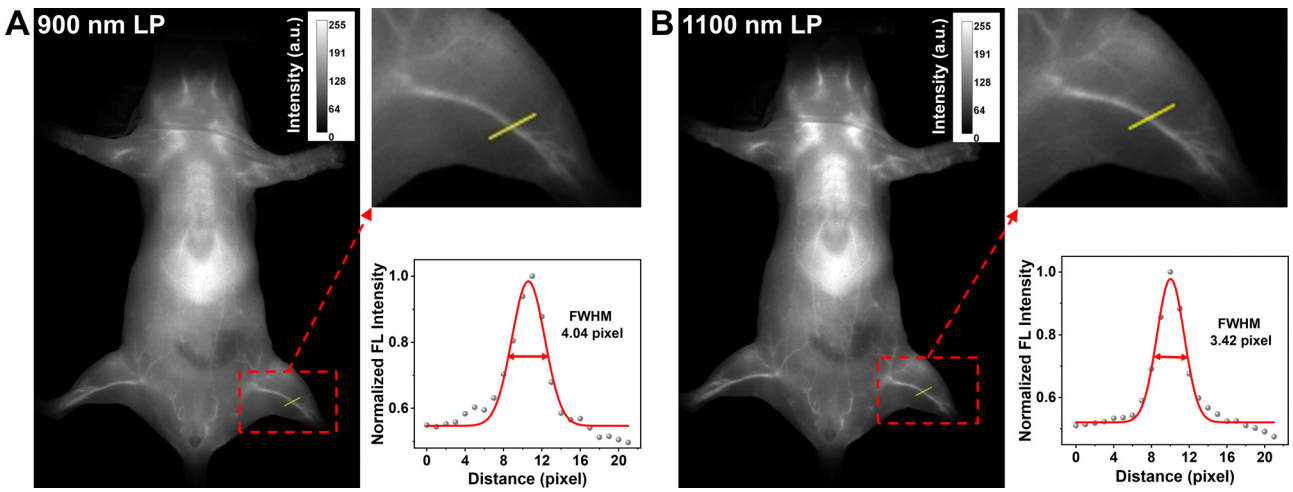

Fig. 6 *In vivo* NIR-II fluorescence imaging of whole-body mouse vasculature using BTP-2TCF NPs. (A) Vascular imaging using a 900 nm LP filter with corresponding FWHM analysis. (B) Vascular imaging using a 1100 nm LP filter with corresponding FWHM analysis.

the blood vessels show that the full width at half-maximum (FWHM) decreases from 4.04 pixels with a 900 nm LP filter to 3.42 pixels with a 1100 nm LP filter, highlighting the superior imaging resolution attainable in the NIR-II window.

These results highlight the potential of BTP-2TCF NPs for fluorescence imaging-guided *in vivo* phototherapy. NIR-II fluorescence images of 4T1 tumor-bearing mice are acquired at various time points post-injection (Fig. 7A). The fluorescence intensity at the tumor site gradually increases, reaching a maximum at 36 hours post-injection (Fig. 7B), indicating efficient tumor accumulation and identifying the optimal time window for phototherapy. At this point, major organs and tumor tissues are excised for *ex vivo* fluorescence imaging. As shown in Fig. 7C and D, the tumor exhibits strong NIR-II fluorescence, comparable to that of the liver, confirming the robust tumor accumulation capability of BTP-2TCF NPs.

To evaluate phototherapeutic anticancer performance *in vivo*, 4T1 tumors in mice are irradiated with an 808 nm laser 36 hours post-injection. Infrared thermal imaging revealed a rapid temperature increase to ~57 °C in the BTP-2TCF NPs group, while the PBS control group showed only a modest rise of ~4 °C (Fig. 7E and F). Tumor growth inhibition was subsequently assessed (Fig. S32 and Fig. 7G–I). Mice treated with BTP-2TCF NPs followed by laser irradiation exhibited significant tumor ablation, attributed to the combined photothermal and photodynamic effects. In contrast, tumors in the PBS,

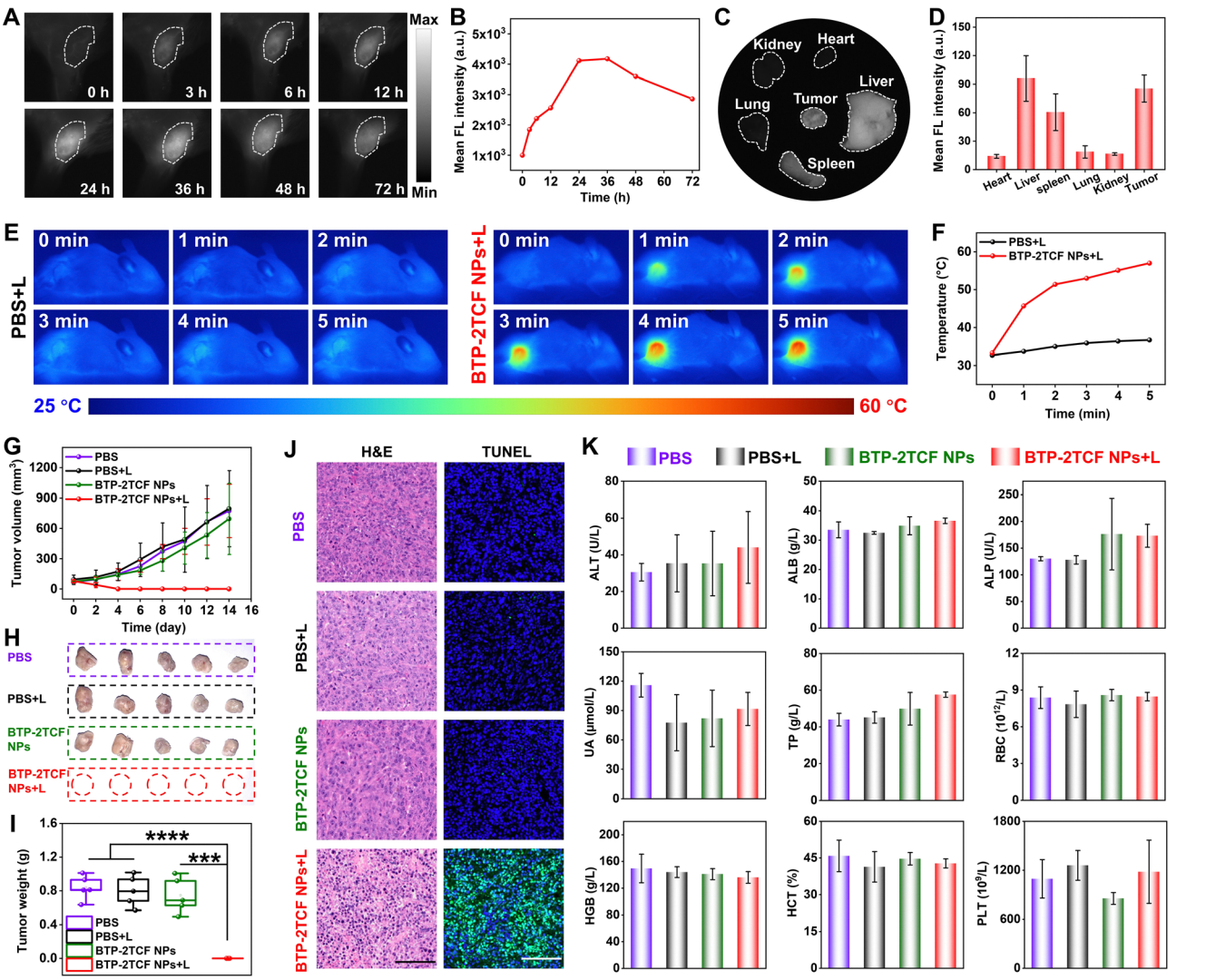

Fig. 7 *In vivo* NIR-II FLI, anticancer performance and biocompatibility of BTP-2TCF NPs. (A) NIR-II FLI images of tumor-bearing mice at various time points following intravenous administration of BTP-2TCF NPs. (B) Quantitative fluorescence intensities of tumors over time post-injection. (C) *Ex vivo* NIR-II FLI images of tumors and major organs collected at 36 h post-injection. (D) Quantification of fluorescence intensities of tumors and organs collected at 36 h post-injection. (E) Infrared thermal images of tumor-bearing mice under 808 nm laser irradiation (0.5 W cm^{-2}) for 5 minutes in PBS + L and BTP-2TCF NPs + L groups. (F) Corresponding temperature changes in the tumor region during irradiation. (G) Tumor volume progression in different treatment groups over 14-day period (n = 5). (H) Photographs of excised tumors from each treatment group (n = 5). (I) Tumor weights of mice in various treatment groups (n = 5). (J) Histological analysis of tumor tissues using H & E and TUNEL in various treatment groups. Scale bar: 100 μm. (K) Blood analysis of mice from various treatment groups after 14 days of treatment. Data are presented as mean ± standard deviation (n = 4).

PBS + L, and BTP-2TCF NPs-only groups continued to grow, indicating that both NPs and laser irradiation are essential for therapeutic efficacy. Throughout the treatment period, mouse body weights were monitored every two days. All groups showed similar trends with modest weight gain, suggesting good systemic tolerance and biosafety of BTP-2TCF NPs (Fig. S33).

To further assess therapeutic efficacy and biocompatibility, histological and hematological analyses are performed. Hematoxylin and eosin (H&E) staining of tumor tissues from the BTP-2TCF NPs + L group reveals severe tumor cell destruction necrosis, which is absent in other groups (Fig. 7J). Terminal deoxynucleotidyl transferase dUTP nick end labeling (TUNEL) staining further confirms significant apoptosis in the treated tumors, validating the effectiveness of the combined phototherapy. Moreover, H&E staining of major organs, including the heart, liver, spleen, lung, and kidney (Fig. S34), indicates consistent tissue morphology across all groups, suggesting no observable organ damage. Finally, blood biochemistry and complete blood count analysis reveal no significant differences between the BTP-2TCF NPs + L group and control groups (Fig. 7K), confirming negligible hepatotoxicity, nephrotoxicity, and overall systemic toxicity.

All animal experiments were performed in accordance with the guidelines approved by the ethics committee of Beijing Institute of Technology with license number BIT-EC-SCXK 2019-0010-228.

3. Conclusions

In this study, a novel planar-TCF-rotor-based NIR-II fluorophore with quenching-resistant performance for photodynamic cancer theranostics was developed. The resulting BTP-2TCF NPs show enhanced NIR-II PLQY and significantly increased ROS generation under 808 nm laser irradiation. This improvement is likely attributed to the restricted intramolecular motion of the TCF rotor, which limits non-radiative energy dissipation. Moreover, BTP-2TCF NPs demonstrate a high molar extinction coefficient, surpassing that of conventional quenching-resistant fluorophores. Combined with their photothermal capabilities, these NPs achieve superior *in vitro* and *in vivo* NIR-II fluorescence imaging-guided tumor phototherapy. We believe that this molecular design strategy offers valuable insights for the development of next-generation quenching-resistant NIR-II fluorophores.

While this work presents a promising planar rotor design, certain limitations remain. The lack of high-quality single crystals hindered direct structural analysis of BTP-2TCF in the aggregated state, likely due to conformational heterogeneity from TCF rotation. Molecular dynamics simulations were employed to explore rotor behavior, but the results could not fully account for the experimental observations, reflecting current challenges in modeling such flexible systems. Additionally, *in vivo* experiments were limited to BTP-2TCF NPs, as differences in NPs–biomolecule interactions and tumor targeting complicate direct benchmarking. These limitations will be progressively addressed in future studies to further refine the design and application of high-performance NIR-II phototheranostic agents.

Conflicts of interest

The authors declare no competing financial interest.

Data availability

The data supporting this article have been included as part of the supplementary information (SI). Supplementary information: methods and materials and the characterization of targeted fluorophores and their nanoparticles. See DOI: https://doi.org/10.1039/d6mh00067c.

Acknowledgements

C.-S. L. acknowledges the support from the Research Grants Council of Hong Kong Special Administrative Region, General Research Fund (Project No. CityU 11318322). K.-T. W. acknowledges the support from the National Science and Technology Council (NSTC-110-2113-M-002-008-MY3), Taiwan. J. Z. would like to acknowledge financial support from the National Natural Science Foundation of China (No. 32371442) and the Beijing Natural Science Foundation (No. 7252289). J. Z. would also like to thank Biological & Medical Engineering Core Facilities (Beijing Institute of Technology) for providing advanced equipment.

References

1 L. Chen, M. Peng, Y. Ouyang, J. Chen, H. Li, M. Wu, R. Qu, W. Zhou, C. Zhang, Y. Jiang, S. Xu, W. Wu, X. Jiang and X. Zhen, *J. Am. Chem. Soc.*, 2025, **147**, 17330–17341.
2 J. Liu, P. Cheng, C. Xu and K. Pu, *Nat. Biomed. Eng.*, 2025, **9**, 618–637.
3 J. Song, H. Wang, X. Meng, W. Li and J. Qi, *Nat. Commun.*, 2024, **15**, 10395.
4 M. Chen, Y. Sun and H. Liu, *Interdiscip. Med.*, 2023, **1**, e20220012.
5 L. Zhang, J. Li, Y. Zhang, W. Dai, Y. Zhang, X. Gao, M. Liu, H. Wu, X. Huang, Y. Lei and D. Ding, *Nat. Commun.*, 2025, **16**, 3970.
6 W. Xu, D. Wang and B. Z. Tang, *Angew. Chem., Int. Ed.*, 2021, **60**, 7476–7487.
7 J. Cui, F. Zhang, D. Yan, T. Han, L. Wang, D. Wang and B. Z. Tang, *Adv. Mater.*, 2023, **35**, 2302639.
8 D. Yan, Y. Huang, J. Zhang, Q. Wu, G. Song, J. Ji, Q. Jin, D. Wang and B. Z. Tang, *J. Am. Chem. Soc.*, 2023, **145**, 25705–25715.
9 T. Huang, K. Yang, W. Hu, L. Feng, Z. Wu, H. Chen, J. Wang and Z. Zeng, *Chem*, 2025, **11**, 102621.
10 D. Yan, X. Li, H. Wang, B. Li, W. Wang, Y. Liao, B. Z. Tang and D. Wang, *Nat. Protoc.*, 2025, 1–26.

11 Y. Sun, F. Qu, R. Geng, W. Xiao, D. Bi, B. Xiong, Y. Liu, J. Zhu and X. Chen, *ACS Nano*, 2024, **18**, 32126–32144.
12 Y. Wan, W. Chen, Y. Liu, K. W. Lee, Y. Gao, D. Zhang, Y. Li, Z. Huang, J. Luo and C. S. Lee, *Adv. Mater.*, 2024, **36**, 2405966.
13 K. W. Lee, Y. Wan, Z. Huang, Q. Zhao, S. Li and C. S. Lee, *Adv. Mater.*, 2024, **36**, 2306492.
14 B. Jia, Y. Liu, X. Geng, Y. Li, C. Zhang, Y. Qu, X. Liu, M. Zhao, Y. Yang and W. Li, *Research*, 2025, **8**, 0732.
15 Q. Lan, P. Yu, K. Yan, X. Li, F. Zhang and Z. Lei, *J. Am. Chem. Soc.*, 2022, **144**, 21010–21015.
16 L. Huang, J. Ming, Z. Wang, J. Wu, B. Yun, A. Liang, Y. Fan and F. Zhang, *Adv. Mater.*, 2025, 2420329.
17 Z. Xu, Y. Jiang, M. Fan, S. Tang, M. Liu, W. C. Law, C. Yang, M. Ying, M. Ma and B. Dong, *Adv. Opt. Mater.*, 2021, **9**, 2100859.
18 C. Li, G. Chen, Y. Zhang, F. Wu and Q. Wang, *J. Am. Chem. Soc.*, 2020, **142**, 14789–14804.
19 Y. Zhu, F. Wu, B. Zheng, Y. Yang, J. Yang and H. Xiong, *Nano Lett.*, 2024, **24**, 8287–8295.
20 D. Barman, K. Narang, R. Parui, N. Zehra, M. N. Khatun, L. R. Adil and P. K. Iyer, *Aggregate*, 2022, **3**, e172.
21 H. Lu, J. Mack, Y. Yang and Z. Shen, *Chem. Soc. Rev.*, 2014, **43**, 4778–4823.
22 M. Al Kobaisi, S. V. Bhosale, K. Latham, A. M. Raynor and S. V. Bhosale, *Chem. Rev.*, 2016, **116**, 11685–11796.
23 Y. Xu, P. Zhang, A. Gao, R. Xu, Z. Wang, Q. Shen, Z. Zhao, L. Meng and D. Dang, *Mater. Chem. Front.*, 2023, **7**, 828–845.
24 W. Xi, P. Xiao, H. Huang, Y. Hu and X. Huang, *Dyes Pigm.*, 2024, 112412.
25 Y. Li, S. Liu, H. Ni, H. Zhang, H. Zhang, C. Chuah, C. Ma, K. S. Wong, J. W. Lam and R. T. Kwok, *Angew. Chem., Int. Ed.*, 2020, **132**, 12922–12926.
26 P. Rybczynski, T. Muzioł, A. Kaczmarek-Kedziera and B. Osmialowski, *J. Phys. Chem. C*, 2024, **128**, 5651–5658.
27 Z. Zhu, J. Qian, X. Zhao, W. Qin, R. Hu, H. Zhang, D. Li, Z. Xu, B. Z. Tang and S. He, *ACS Nano*, 2016, **10**, 588–597.
28 Y. Cai, X. Ji, Y. Zhang, C. Liu, Z. Zhang, Y. Lv, X. Dong, H. He, J. Qi and Y. Lu, *Aggregate*, 2023, **4**, e277.
29 H. Huang, L. Liu, J. Wang, Y. Zhou, H. Hu, X. Ye, G. Liu, Z. Xu, H. Xu and W. Yang, *Chem. Sci.*, 2022, **13**, 3129–3139.
30 X. Ma, W. Chi, X. Han, C. Wang, S. Liu, X. Liu and J. Yin, *Chin. Chem. Lett.*, 2021, **32**, 1790–1794.
31 X. Liu, J. Liu and C. Zhu, *Matter*, 2022, **5**, 3583–3585.
32 M. Yang, X. Ou, J. Li, J. Sun, Z. Zhao, J. W. Lam, J. Fan and B. Z. Tang, *Angew. Chem., Int. Ed.*, 2024, **63**, e202407307.
33 H. Liu, N. Yan, H. Bai, R. T. Kwok and B. Z. Tang, *Exploration*, 2022, **2**, 20210053.
34 M. M. Lee, E. Y. Yu, J. H. Chau, J. W. Lam, R. T. Kwok and B. Z. Tang, *Adv. Mater.*, 2024, 2407707.
35 D. D. La, S. V. Bhosale, L. A. Jones and S. V. Bhosale, *ACS Appl. Mater. Interfaces*, 2017, **10**, 12189–12216.
36 J. Y. Chen, G. Kadam, A. Gupta, Anuradha, S. V. Bhosale, F. Zheng, C. H. Zhou, B. H. Jia, D. S. Dalal and J. L. Li, *Chem. – Eur. J.*, 2018, **24**, 14668–14678.
37 H. Gao, Y. Yao, C. Li, J. Zhang, H. Yu, X. Yang, J. Shen, Q. Liu, R. Xu and X. Gao, *Angew. Chem., Int. Ed.*, 2024, **136**, e202400372.
38 P. Xin, H. Xie, Z. Liu, Z. Tian, J. Cai, Z. Zhao, Z. Qiu, J. Zhang and B. Z. Tang, *ACS Nano*, 2025, **19**, 28813–28826.
39 H. Shen, F. Sun, X. Zhu, J. Zhang, X. Ou, J. Zhang, C. Xu, H. H. Sung, I. D. Williams and S. Chen, *J. Am. Chem. Soc.*, 2022, **144**, 15391–15402.
40 J. Li, G. Q. Zhang, Y. Zhang, Y. Tang, D. Ding, W. Li and Q. Liu, *Adv. Funct. Mater.*, 2023, **33**, 2212380.
41 Y. Qin, N. Balar, Z. Peng, A. Gadisa, I. Angunawela, A. Bagui, S. Kashani, J. Hou and H. Ade, *Joule*, 2021, **5**, 2129–2147.
42 M. Li, Z. Lu, J. Zhang, L. Chen, X. Tang, Q. Jiang, Q. Hu, L. Li, J. Liu and W. Huang, *Adv. Mater.*, 2023, **35**, 2209647.
43 B. Lu, Z. Zhang, D. Jin, X. Yuan, J. Wang, Y. Ding, Y. Wang and Y. Yao, *Chem. Commun.*, 2021, **57**, 12020–12023.
44 C. Li, J. Du, G. Jiang, J. Gong, Y. Zhang, M. Yao, J. Wang, L. Wu and B. Z. Tang, *Nat. Commun.*, 2024, **15**, 5832.
45 F. Wan, H. Wang, Y. Gu, G. Fan, S. Hou, J. Yu, M. Wang, F. He and L. Tian, *Chem. – Eur. J.*, 2024, **30**, e202303502.
46 Y. Zhu, H. Lai, Y. Gu, Z. Wei, L. Chen, X. Lai, L. Han, P. Tan, M. Pu and F. Xiao, *Adv. Sci.*, 2024, **11**, 2307569.
47 P.-A. Bouit, E. Di Piazza, S. Rigaut, B. Le Guennic, C. Aronica, L. Toupet, C. Andraud and O. Maury, *Org. Lett.*, 2008, **10**, 4159–4162.
48 M. D. H. Bhuiyan, M. Ashraf, A. Teshome, G. J. Gainsford, A. J. Kay, I. Asselberghs and K. Clays, *Dyes Pigm.*, 2011, **89**, 177–187.
49 X. Hao, M. Gao, R. Zhang, Y. Tang, X. Mu, Y. Zhao, Y. Lu and X. Zhou, *Adv. Funct. Mater.*, 2025, **35**, 2416317.
50 G. Noirbent, C. Pigot, T.-T. Bui, S. Péralta, M. Nechab, D. Gigmes and F. Dumur, *Dyes Pigm.*, 2021, **184**, 108807.
51 D. Zhang, W. Chen, J. Zou and J. Luo, *Chem. Mater.*, 2021, **33**, 3702–3711.
52 M. Bruschi, P. A. Limacher, J. R. Hutter and H. P. Lüthi, *J. Chem. Theory Comput.*, 2009, **5**, 506–514.
53 X. Wang, X. Yang, G. Jiang, Z. Hu, T. Liao, G. Wang, X. Zhang, X. He, J. Zhang and J. Zhang, *Angew. Chem., Int. Ed.*, 2024, **63**, e202404142.
54 J. Zhang, W. Liu, Y. Liu, J. Zhang, P. Gao, L. Zheng, F. Xu, G. Jin and B. Z. Tang, *Adv. Mater.*, 2023, **35**, 2306616.
55 J. Li, N. Niu, D. Wang, J. Zhu, X. Li, Q. Kong, B. Zhong Tang and D. Wang, *Angew. Chem., Int. Ed.*, 2025, **64**, e202413219.
56 V. Ragavendran and S. Muthunatesan, *Vib. Spectrosc.*, 2017, **92**, 35–45.
57 N. A. Derevyanko, A. A. Ishchenko and A. V. Kulinich, *Phys. Chem. Chem. Phys.*, 2020, **22**, 2748–2762.
58 W. Chen, T. Liu, J. Zou, D. Zhang, M. K. Tse, S. W. Tsang, J. Luo and A. K. Y. Jen, *Adv. Mater.*, 2024, **36**, 2306089.
59 G. Midekessa, K. Godakumara, J. Ord, J. Viil, F. Lättekivi, K. Dissanayake, S. Kopanchuk, A. Rinken, A. Andronowska and S. Bhattacharjee, *ACS omega*, 2020, **5**, 16701–16710.
60 Z. Zhang, X. Fang, Z. Liu, H. Liu, D. Chen, S. He, J. Zheng, B. Yang, W. Qin and X. Zhang, *Angew. Chem., Int. Ed.*, 2020, **59**, 3691–3698.

61 Y. Nosaka and A. Y. Nosaka, *Chem. Rev.*, 2017, **117**, 11302–11336.
62 K. W. Lee, Y. Gao, S. H. Chou, Y. Wan, A. C. H. Hsu, J. H. Tan, Y. Li, Z. Guan, H. Chen and S. Li, *Adv. Funct. Mater.*, 2024, **34**, 2407317.
63 J. Zhang, C. Yang, R. Zhang, R. Chen, Z. Zhang, W. Zhang, S. H. Peng, X. Chen, G. Liu and C. S. Hsu, *Adv. Funct. Mater.*, 2017, **27**, 1605094.
64 Y. Wan, G. Lu, W.-C. Wei, Y.-H. Huang, S. Li, J.-X. Chen, X. Cui, Y.-F. Xiao, X. Li and Y. Liu, *ACS Nano*, 2020, **14**, 9917–9928.
65 H. Ren, J. Liu, F. Su, S. Ge, A. Yuan, W. Dai, J. Wu and Y. Hu, *ACS Appl. Mater. Interfaces*, 2017, **9**, 3463–3473.
66 P. Majumdar, R. Nomula and J. Zhao, *J. Mater. Chem. C*, 2014, **2**, 5982–5997.
67 A. V. Talyzin, V. L. Solozhenko, O. O. Kurakevych, T. Szabó, I. Dékány, A. Kurnosov and V. Dmitriev, *Angew. Chem.*, 2008, **120**, 8392–8395.
68 T.-H. Kim, E. K. Jeon, Y. Ko, B. Y. Jang, B.-S. Kim and H.-K. Song, *J. Mater. Chem. A*, 2014, **2**, 7600–7605.
69 R. Yang, L. Ding, W. Chen, L. Chen, X. Zhang and J. Li, *Macromolecules*, 2017, **50**, 1610–1617.
70 L. Zhu, W. Zhong, C. Qiu, B. Lyu, Z. Zhou, M. Zhang, J. Song, J. Xu, J. Wang and J. Ali, *Adv. Mater.*, 2019, **31**, 1902899.
71 G. Dyadyusha and A. Ishchenko, *J. Appl. Spectrosc.*, 1979, **30**, 746–750.
72 S. G. Stenspil and B. W. Laursen, *Chem. Sci.*, 2024, **15**, 8625–8638.
73 Z. Zhao, C. Chen, W. Wu, F. Wang, L. Du, X. Zhang, Y. Xiong, X. He, Y. Cai and R. T. Kwok, *Nat. Commun.*, 2019, **10**, 768.
74 Y. Zhu, R. Zhang, X. M. Cai, L. Zhang, B. Wu, H. Tan, K. Zhou, H. Wang, Y. Liu and Y. Luo, *Adv. Healthcare Mater.*, 2025, **14**, 2404505.
75 Q. Wang, J. Xu, R. Geng, J. Cai, J. Li, C. Xie, W. Tang, Q. Shen, W. Huang and Q. Fan, *Biomaterials*, 2020, **231**, 119671.
76 S. Wang, L. Shang, L. Li, Y. Yu, C. Chi, K. Wang, J. Zhang, R. Shi, H. Shen and G. I. Waterhouse, *Adv. Mater.*, 2016, **28**, 8379–8387.
77 L. Yang, B. Huang, S. Hu, Y. An, J. Sheng, Y. Li, Y. Wang and N. Gu, *Nano Res.*, 2022, **15**, 4285–4293.
78 W. Hu, P. N. Prasad and W. Huang, *Acc. Chem. Res.*, 2020, **54**, 697–706.
79 S. Chen, Y. Pan, K. Chen, P. Chen, Q. Shen, P. Sun, W. Hu and Q. Fan, *Angew. Chem., Int. Ed.*, 2023, **135**, e202215372.
80 H. Ma, S. Long, J. Cao, F. Xu, P. Zhou, G. Zeng, X. Zhou, C. Shi, W. Sun and J. Du, *Chem. Sci.*, 2021, **12**, 13809–13816.
81 Y. Liang, Y. Pan, L. Chen, P. Li, M. Xu, H. Zhou, X. Lu, W. Hu, C. Yin and Q. Fan, *Angew. Chem., Int. Ed.*, 2024, **136**, e202408861.
82 X. Hu, Z. Fang, F. Sun, C. Zhu, M. Jia, X. Miao, L. Huang, W. Hu, Q. Fan, Z. Yang and W. Huang, *Angew. Chem., Int. Ed.*, 2024, **63**, e202401036.
83 Y. Zhu, H. Lai, H. Guo, D. Peng, L. Han, Y. Gu, Z. Wei, D. Zhao, N. Zheng and D. Hu, *Angew. Chem., Int. Ed.*, 2022, **61**, e202117433.

